Available online at www.sciencedirect.com
ScienceDirect
International Journal of Heat and Mass Transfer 51 (2008) 2214–2226
International Journal of HEAT and MASS TRANSFER
www.elsevier.com/locate/ijhmt

A porous model for the square pin-fin heat sink situated in a rectangular channel with laminar side-bypass flow

Tzer-Ming Jeng *

Department of Mechanical Engineering, Air Force Institute of Technology, GangShan 820, Taiwan, ROC

Received 13 June 2007; received in revised form 1 November 2007
Available online 21 February 2008

Abstract

This work illustrates the compact heat sink simulations in forced convection flow with side-bypass effect. Conventionally, the numerical study of the fluid flow and heat transfer in finned heat sinks employs the detailed model that spends a lot of computational time. Therefore, some investigators begin to numerically study such problem by using the compact model (i.e. the porous approach) since the regularly arranged fin array can be set as a porous medium. The computations of the porous approach model will be faster than those of the detailed mode due to the assumption of the volume-averaging technique. This work uses the Brinkman–Forchheimer model for fluid flow and two-equation model for heat transfer. A configuration of in-line square pin-fin heat sink situated in a rectangular channel with fixed height ($H = 23.7$ mm), various width and two equal-spacing bypass passages beside the heat sink is successfully studied. The pin-fin arrays with various porosities ($\varepsilon = 0.358$–0.750) and numbers of pin-fins ($n = 25$–81), confined within a square spreader whose side length (L) is 67 mm, are employed. The numerical results suggest that, within the range of present studied parameters ($0.358 \leqslant \varepsilon \leqslant 0.750$, $25 \leqslant n \leqslant 81$ and $1 \leqslant W/L \leqslant 5$), the pin-fin heat sink with $\varepsilon = 0.750$ and $n = 25$ is the optimal cooling configuration based on the maximum ratio of Nusselt number to dimensionless pumping power ($Nu/(\Delta P \times Re^3)$). Besides, based on medium $Nu/(\Delta P \times Re^3)$ value and suitable channel size, $W/L = 2$–3 is suggested as the better size ratio of channel to heat sink.

Keywords: Compact model; Porous approach; Pin-fin heat sink; Bypass effect

1. Introduction

Given their inexpensive and simple structure, pin-fins have extensive applications. Applications of pin-fins in the cooling configuration of a channel with cross flow include the internal cooling of turbine blades, the cooling of electronic components and various other heat exchange devices. The affecting factors on the thermal performance of such systems include the velocity of fluid flow, the thermal properties of the fluid and of the pin-fins, the relative fin height, the cross-sectional shape of the pin-fins, the relative inter-fin pitch, the arrangement of the pin-fins and the bypass effect. Many researchers have considered the effects of the aforementioned parameters on heat transfer of pin-fins. Most of the studies focused on the bypass effect have the configuration with the tip shroud clearance above the pin-fin array [1–6]. It is because that the tip bypass generally has greater influence on the thermal and hydraulic performance for the systems of pin-fin heat sinks. Another reason for focusing on the tip clearance bypass is that the tip bypass can be changed at a late design stage whereas the channel width most often is predecided by the choice of PCB width and therefore cannot be changed at the end of the design cycle. However, the fact is that the system with the side clearance bypass also influences the thermal and hydraulic performance of pin-fin heat sinks but induces little attention.

This work is to discuss putting a pin-fin heat sink into a rectangular channel with bypass passages of the same width on both sides. Fig. 1 is a typical flow field of such cooling system. Considering the symmetric configuration

* Tel.: +886 7 6256040; fax: +886 4 7357193.
E-mail addresses: tm.jeng@msa.hinet.net, t_m_jeng@yahoo.com.tw

0017-9310/$ - see front matter © 2007 Elsevier Ltd. All rights reserved.
doi:10.1016/j.ijheatmasstransfer.2007.11.018

Nomenclature

a_{fs}	dissipation area per unit volume (m^2/m^3)
C_F	inertial coefficient of the pin-fin heat sink
C_p	specific heat at constant pressure (J/kg/°C)
d	thickness of the pin-fin (m)
Da	Darcy number, $Da = K/H^2$
D_h	hydraulic diameter of the channel (m), $D_h = 4WH/(2W + 2H)$
h	total heat transfer coefficient ($W/m^2/°C$)
h_{fs}	heat transfer coefficient between fluid stream and pin-fins ($W/m^2/°C$)
H	height of the pin-fin or width of the channel (m)
K	permeability of the pin-fin heat sink (m^2)
k	thermal conductivity (W/m/°C)
L	length of the square heat sink (m)
L_{in}	length of channel upstream from the pin-fin heat sink (m)
L_{out}	length of channel downstream from the pin-fin heat sink (m)
Nu	Nusselt number, $Nu = hD_h/k_f$
p	pressure (Pa)
Pr	Prandtl number, $Pr = (\mu C_p)_f/k_f$
q_w	heat flux from the heated base (W/m^2)
Re	Reynolds number based on D_h, $Re = \rho_f u_i D_h/\mu_f$
Re_H	Reynolds number based on H, $Re = \rho_f u_i H/\mu_f$
S_L	center-to-center longitudinal distance between the adjacent pin-fins (m)
S_T	center-to-center transverse distance between the adjacent pin-fins (m)
T	temperature (°C)
u	velocity in streamwise direction (m/s)
U	dimensionless velocity in streamwise direction, $U = u/u_i$
U_M	dimensionless magnitude of the velocity, $U_M = \sqrt{u^2 + v^2}/u_i$
v	velocity in transverse direction (m/s)
V	dimensionless velocity in transverse direction, $V = v/u_i$
W	width of the channel (m)
x, y	Cartesian coordinates (m)
X, Y	dimensionless Cartesian coordinates, $X = x/H$ and $Y = y/H$
ΔP	dimensionless pressure drop across the pin-fin heat sink, $\Delta P = (p_i - p_e)/(\rho_f u_i^2)$

Greek symbols

ε	porosity of the pin-fin heat sink (i.e. the total void volume divided by the total volume occupied by the solid matrix and the void volume)
μ	viscosity (kg/m/s)
θ	dimensionless temperature, $\theta = (T - T_i)/(q_w H/k_f)$
ρ	density (kg/m^3)
ω	vorticity
Ψ	stream function

Subscripts

b	based on bulk mean temperature
e	at channel exit
f	fluid
i	at channel inlet
s	solid
w	channel wall

Superscript

*	effective

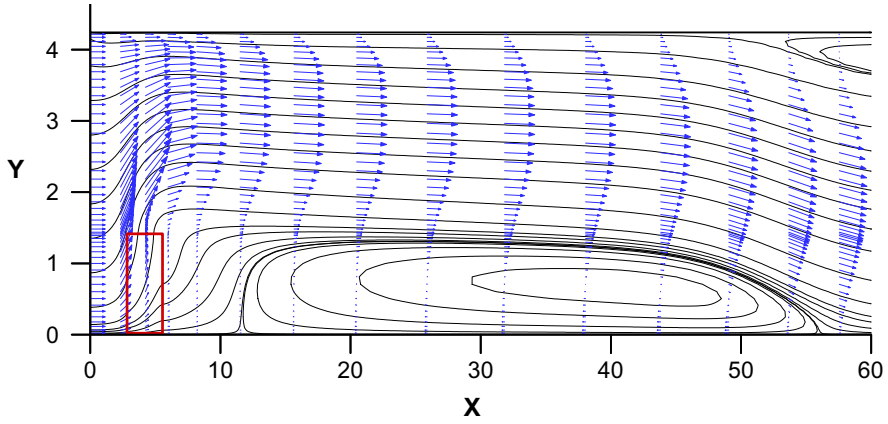

Fig. 1. The typical flow field.

of the present system, it only shows the upper half of the whole flow field. The air flow passing through the heat sink is regarded as the major coolant and affects the cooling performance of the heat sink. Its amount depends on the permeability and inertial coefficient of the pin-fin heat sink, as well as the size proportion of the channel to the heat sink.

Moreover, owing to the airflow passing through the heat sink, the recirculation zone is not generated immediately after the heat sink, but at a far place in the downstream. Fu et al. [7] numerically investigated the fluid flow and heat transfer in the channel with a porous block on the bottom wall, and also found this kind of fluid flow characteristics.

Conventionally, the numerical study of the fluid flow and heat transfer in finned heat sinks employs the detailed model that a three-dimensional calculation is involved. Since 3D numerical computations require substantial CPU time, some investigators begin to numerically study such problem by using the compact model (i.e. the porous approach) as the regularly arranged fin array can be set as a porous medium. The computations of the porous approach model will be faster than those of the detailed mode due to the assumption of the volume-averaging technique. Morega et al. [8], and Narasimhan and Majdalani [9] explored the fluid flow and heat transfer in longitudinal plate fin array by using the porous approach model. These studies assumed the local thermal equilibrium condition between the fluid and fins, and employed the one-equation model for the energy equation. Kim and Kim [10,11] modeled the longitudinal plat fin heat sink as a fluid-saturated porous medium. They provided the analytical solutions for both velocity and temperature profiles, based on the modified Darcy model for fluid flow and the two-equation model for heat transfer. Yu and Joshi [12] experimentally and numerically investigated the enhancement of combined natural convection, conduction and radiation heat transfer of pin-fin heat sink in an enclosed box. The numerical simulation in their work utilized the Brinkman–Forchheimer model for fluid flow and one-equation model for heat transfer.

Before fluid flow and heat transfer can be numerically analyzed using the compact model (i.e. the porous approach), the porous characteristics, such as the permeability (K) and the inertial coefficient (C_F) and the solid-to-fluid heat transfer coefficient (h_{fs}), need to be determined. However, due to the lack of systematical studies on the porous transport properties of the square pin-fin heat sinks, most of the previous similarity work between finned heat sinks and porous media focused on the configuration of longitudinal plate fins. Fortunately, in the past decade, the porous transport properties of the square pin-fin heat sink attracted some investigators. You and Chang [13,14] employed experimental data to numerically determine the porous flow and thermal characteristics for a square pin-fin channel flow, by applying the non-Darcian model and two-equation model. Kim et al [15] modifies the method of You and Chang [13,14] to model the pin-fin heat sink as a porous medium. Recently, Jeng and Tzeng [16] presented a novel semi-empirical model for estimating the permeability and inertial coefficient of pin-fin heat sinks. The forms of correlations for the permeability and inertial coefficient of pin-fin heat sinks were firstly derived theoretically, then a series of pressure drop tests were performed for modifying those correlations. The above studies contribute to compact model simulation of the pin-fin heat sink in the convection flow.

This work illustrates the compact heat sink simulations in forced convection flow with side-bypass effect. The Brinkman–Forchheimer model is used for fluid flow and two-equation model for heat transfer. A configuration of in-line square pin-fin heat sink situated in a rectangular channel with fixed height ($H = 23.7$ mm), various width (W) and two equal-spacing bypass passages beside the heat sink is successfully studied. The pin-fin arrays with various porosities ($\varepsilon = 0.358$–0.750) and numbers of pin-fins ($n = 25$–81), confined within a square spreader whose side length (L) is 67 mm, are employed. In the present investigation, the basic interaction phenomena between the pin-fin heat sink and the fluid region within the channel are studied. Furthermore, the effects of various parameters, such as the porosity (ε), the number of pin-fins (n) and the wide size proportion of the channel to the heat sink (W/L), on the fluid flow and heat transfer are analyzed.

2. Numerical model

2.1. Governing equations

Fig. 2 is a physical configuration, which sets the regularly arranged pin-fins as porous media. The center-to-center longitudinal distance between the adjacent pin-fins is S_L, the center-to-center transverse distance is S_T, the number of pin-fins is n, the thickness of each square pin-fin is d, the size of pin-fin heat sink is $L \times L \times H$, and the cross-section size of the channel is $W \times H$. The heat flux is firstly transmitted upwards from the paper surface through the pin-fins by heat conduction, and then transmitted to the air passing through the heat sink from the extended surface of the pin-fins by heat convection. If the heat transfer on the end-wall surface of the pin-fin heat sink is unconsidered, the heat dissipated from pin-fins can be regarded as the heat generated in the porous media of pin-fins. Therefore, the present study can be simplified to be two-dimensional problem. Other assumptions are as follows: (1) the porous medium is homogenous and isotropic; (2) the fluid flow is steady state, laminar and incompressible; (3) the thermophysical properties of the fluid and

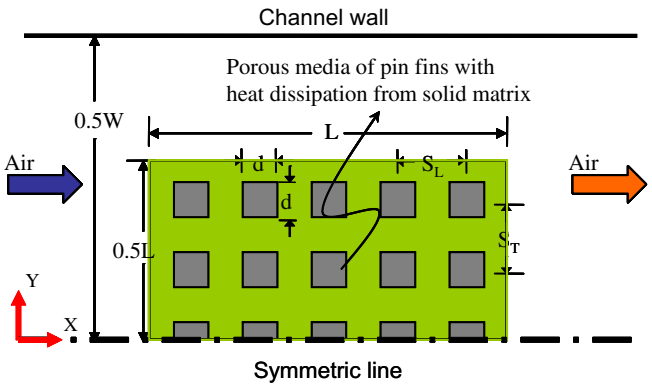

Fig. 2. Physical configuration.

porous media do not depend on temperature. Besides, the dimensionless parameters are as follows:

$$X=\frac{x}{H},\quad Y=\frac{y}{H},\quad U=\frac{u}{u_{\mathrm{i}}},\quad V=\frac{v}{u_{\mathrm{i}}},$$
$$Pr=\frac{\mu/\rho_{\mathrm{f}}}{k_{\mathrm{f}}/(\rho C_p)_{\mathrm{f}}},\quad Da=\frac{K}{H^2},$$
$$Re_H=\frac{\rho_{\mathrm{f}}u_{\mathrm{i}}H}{\mu},\quad U_{\mathrm{M}}=\frac{\sqrt{u^2+v^2}}{u_{\mathrm{i}}},\quad \theta=\frac{T-T_{\mathrm{i}}}{q_{\mathrm{w}}H/k_{\mathrm{f}}},\tag{1}$$
$$Nu_{\mathrm{fs}}=\frac{h_{\mathrm{fs}}a_{\mathrm{fs}}H^2}{k_{\mathrm{f}}}$$

where K is the permeability; a_{fs} is the surface area of the fluid–solid interface per unit bulk volume of the pin-fin heat sink; h_{fs} is the heat transfer coefficient between the fluid stream and the solid matrix, and q_{w} is the heat flux on the bottom of the pin-fin heat sink. Furthermore, replacing the velocity components with the vorticity (ω) and the stream function (Ψ),

$$\omega=-\frac{\partial U}{\partial Y}+\frac{\partial V}{\partial X},\quad U=\frac{\partial \Psi}{\partial Y},\quad V=-\frac{\partial \Psi}{\partial X}\tag{2}$$

the dimensionless volume-averaged conservation equations (i.e. the compact model or the porous approach model) can be expressed as follows:

$$-\omega=\frac{\partial^2\Psi}{\partial X^2}+\frac{\partial^2\Psi}{\partial Y^2}\tag{3}$$

$$U\frac{\partial\omega}{\partial X}+V\frac{\partial\omega}{\partial Y}=-\frac{\varepsilon^2}{Re_H\cdot Da}\omega-\frac{\varepsilon^2C_FU_{\mathrm{M}}}{\sqrt{Da}}\omega+\frac{\varepsilon^2C_F}{\sqrt{Da}}\times\left(U\frac{\partial U_{\mathrm{M}}}{\partial Y}-V\frac{\partial U_{\mathrm{M}}}{\partial X}\right)+\frac{\varepsilon}{Re_H}\left(\frac{\partial^2\omega}{\partial X^2}+\frac{\partial^2\omega}{\partial Y^2}\right)\tag{4}$$

$$U\frac{\partial\theta_{\mathrm{f}}}{\partial X}+V\frac{\partial\theta_{\mathrm{f}}}{\partial Y}=\frac{Nu_{\mathrm{fs}}}{Re_H\cdot Pr}(\theta_{\mathrm{s}}-\theta_{\mathrm{f}})+\frac{1}{Re_H\cdot Pr}\frac{k_{\mathrm{f}}^*}{k_{\mathrm{f}}}\times\left(\frac{\partial^2\theta_{\mathrm{f}}}{\partial X^2}+\frac{\partial^2\theta_{\mathrm{f}}}{\partial Y^2}\right)\tag{5}$$

$$0=Nu_{\mathrm{fs}}(\theta_{\mathrm{f}}-\theta_{\mathrm{s}})+\frac{k_{\mathrm{s}}^*}{k_{\mathrm{f}}}\left(\frac{\partial^2\theta_{\mathrm{s}}}{\partial X^2}+\frac{\partial^2\theta_{\mathrm{s}}}{\partial Y^2}\right)+\delta\tag{6}$$

where C_F is the inertial coefficient; ε is the porosity of the pin-fin heat sink (i.e. the total void volume divided by the total volume occupied by the solid matrix and the void volume); k_{s}^* is the effective conductivity of the solid matrix, and k_{f}^* is the effective conductivity of the fluid. Notably, in the clear fluid region, Da is set to infinity and ε to unity. Also, $Nu_{\mathrm{fs}}=k_{\mathrm{s}}^*=0$ and $k_{\mathrm{f}}^*=k_{\mathrm{f}}$. The δ is a function set equal to one to account for heat generation in the porous media of pin-fins and to zero elsewhere.

The relevant empirical coefficients in the present porous medium of pin-fins, such as K, C_F, k_{s}^*, k_{f}^* and h_{fs}, generally do not have universal values. This is because that these empirical coefficients mainly depend on the geometry of the porous medium, the thermal properties of the solid and the fluid, and the flow rate. Moreover, all these empirical coefficients are difficult to measure. This work contributes to build a compact model for pin-fin array by finding the suitable empirical formula of K, C_F, k_{s}^*, k_{f}^* and h_{fs} in the open literature. Firstly, the total effective conductivity k_{e} and the k_{f}^* are derived by using the combination of the parallel and series models [17], and then the k_{s}^* equals the difference between k_{e} and k_{f}^*. The k_{s}^* should be considered in the volume-averaged equations since the disconnected pin-fins enhance the k_{e}. Additionally, the estimation of the K and C_F is based on a semi-empirical model whose details are provided by Jeng and Tzeng [16]. The relevant dimensions and porous properties of pin-fin heat sinks numerically studied herein are shown in Table 1. Finally, the h_{fs} of the square pin-fin heat sink with uniform in-line arrangement is predicted by employing the empirical equations suggested by Kim et al. [15]:

$$h_{\mathrm{fs}}=\frac{\varepsilon k_{\mathrm{f}}}{d}\left(0.36283Re_d^{0.54219}\right)\quad\text{for}\quad Re_d<1000\tag{7}$$

$$h_{\mathrm{fs}}=\frac{\varepsilon k_{\mathrm{f}}}{d}\left(0.04433Re_d^{0.82934}\right)\quad\text{for}\quad Re_d\geqslant 1000\tag{8}$$

where Re_d is defined as $\rho_{\mathrm{f}}u_{\max}d/\mu$; $u_{\max}$ is the average maximum velocity between pin-fins, and d is the pin-fin thickness.

2.2. Boundary conditions

Fig. 3 schematically depicts the numerical domain and the boundary conditions. Roache [18] elucidated the boundary conditions of the vorticity-transport equation. The temperature gradients of the solid phase and the fluid phase along the Y-direction are zero on the insulated and

Table 1
Porous properties of pin-fin heat sinks used herein

In-line square pin-fin heat sink with uniform distributions ($S_{\mathrm{L}}=S_{\mathrm{T}}$), $L=0.067$ m, $H=0.0237$ m					
Test specimens	Sample 1	Sample 2	Sample 3	Sample 4	Sample 5
d (m)	0.00596	0.00496	0.00372	0.00479	0.0067
n	9 × 9	9 × 9	9 × 9	7 × 7	5 × 5
ε	0.358	0.556	0.750	0.750	0.750
K (m^2)	4.37E−08	2.40E−07	1.03E−06	1.63E−06	2.95E−06
C_F	0.0808	0.0785	0.0451	0.0486	0.0543
k_{f}^* (W/m °C)	0.0064	0.0116	0.018	0.018	0.018
k_{s}^* (W/m °C)	0.129	0.0694	0.036	0.036	0.036
a_{fs} (m^2/m^3)	445	381	300	241	181

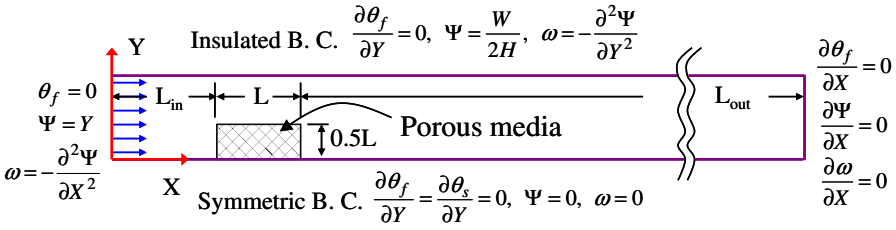

Fig. 3. Computational configuration.

symmetric faces. The fluid is assumed to enter the inlet with a uniform temperature (T_i) and a uniform velocity (u_i). The fluid phase at the exit is assumed to meet the zero diffusion condition since the downstream length L_{out} (=20L) is chosen to be sufficiently long. The relevant boundary conditions are as follows:

$$\theta_f = 0, \quad \Psi = Y, \quad \omega = -\frac{\partial^2 \Psi}{\partial X^2} \quad \text{for the inlet face} \tag{9}$$

$$\frac{\partial \theta_f}{\partial X} = 0, \quad \frac{\partial \Psi}{\partial X} = 0, \quad \frac{\partial \omega}{\partial X} = 0 \quad \text{for the outlet face} \tag{10}$$

$$\frac{\partial \theta_f}{\partial Y} = \frac{\partial \theta_s}{\partial Y} = 0, \quad \Psi = 0, \quad \omega = 0$$
for the bottom symmetric face (11)

$$\frac{\partial \theta_f}{\partial Y} = 0, \quad \Psi = \frac{W}{2H}, \quad \omega = -\frac{\partial^2 \Psi}{\partial Y^2}$$
for the top insulated face (12)

Besides, the interfacial boundary condition plays very important roles in the porous/fluid composite system. This is due to the abrupt change of thermophysical properties, such as the permeability, inertial coefficient and porosity, across the interface. The harmonic mean formulation recommended by Patankar [19] is used to treat these discontinuous characteristics at the porous/fluid surface. Moreover, Huang and Vafai [20] suggested a modified governing equation used across the interface, instead of the Eq. (4), since where the permeability, inertial coefficient and porosity were not constants any more. This modified governing equation for the interfacial region is employed in the present study and its details can be found in Huang and Vafai [20]. Therefore, the single-domain approach can be performed in the present simulations and the continuity of the convection and diffusive fluxes across the interface will be automatically satisfied.

2.3. Numerical procedure and data reduction

This work applies the power-law developed by Patankar [19] to disperse the equations and employs the SIS (strong implicit solver) algorithm proposed by Lee [21] to solve the related dispersal equations. The numerical procedure initially resolves the vorticity and the stream function, and then applies the vorticity and the stream function to resolve the velocity field, which is subsequently substituted into the fluid energy equation. Then, the solid and fluid energy equations are solved and the subsequent solid and fluid temperature fields are obtained. All of the resolutions undergo the grid independence test and convergence test. The large variations in the W/L value (W/L = 1–5) are such that grid systems are separated into various classes to fit the physical model. The grid points, in an X–Y coordinate, are

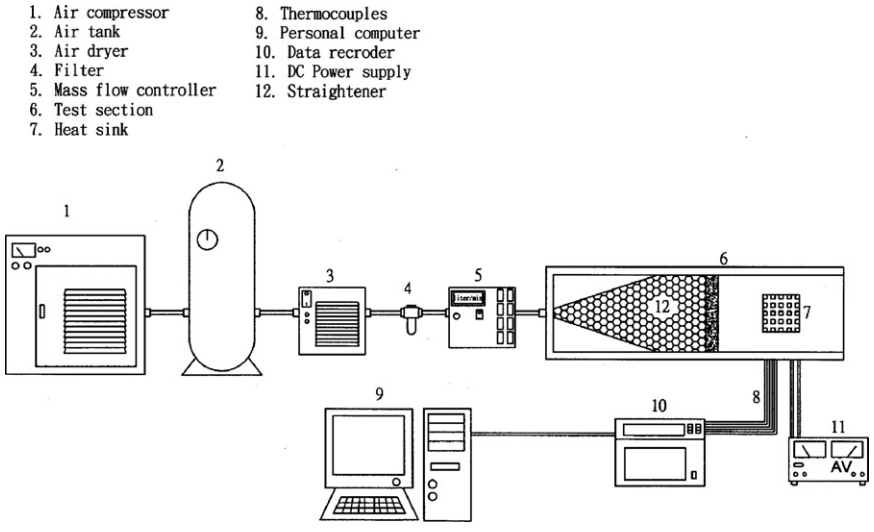

Fig. 4. Experimental setup.

481×21, 481×31, 481×41, 481×51 and 481×61, respectively. The grid size falls as W/L value decreases. The iteration ends when the variables meet the criterion,

$$\sum_{i,j}\left|\frac{F_{i,j}^{n+1}-F_{i,j}^{n}}{F_{i,j}^{n+1}}\right| \leqslant 1\times 10^{-5} \tag{13}$$

where F represents Ψ, ω or θ. The subscripts i and j refer to the ith and the jth grid-cells in the X and Y directions, respectively. The superscript n indicates the nth iteration.

The major parameters of heat transfer performance observed herein are the Reynolds number (Re), the dimensionless pressure drop (ΔP) and the average Nusselt number (Nu), which are defined as follows:

$$Re = \frac{\rho u_{\mathrm{i}} D_{\mathrm{h}}}{\mu} \tag{14}$$

$$\Delta P = \frac{p_{\mathrm{i}}-p_{\mathrm{e}}}{\rho_{\mathrm{f}} u_{\mathrm{i}}^2} = \int_{L_{\mathrm{in}}/H}^{(L_{\mathrm{in}}+L)/H}\left(\frac{1}{ReDa}+\frac{C_F}{\sqrt{Da}}U_{\mathrm{M}}U - \frac{1}{\varepsilon Re}\frac{\partial^2 U}{\partial X^2}+\frac{U}{\varepsilon^2}\frac{\partial U}{\partial X}\right)_{Y=0}\mathrm{d}X \tag{15}$$

$$Nu = \int_0^L\int_0^{L/2} Nu_{x,y}\,\mathrm{d}y\,\mathrm{d}x/(L^2/2) \tag{16}$$

where

$$Nu_{x,y} = \frac{q_{\mathrm{w}}D_{\mathrm{h}}}{(T_{\mathrm{w}}-T_{\mathrm{i}})k_{\mathrm{f}}} = \frac{q_{\mathrm{w}}D_{\mathrm{h}}}{(T_{\mathrm{s}}-T_{\mathrm{i}})k_{\mathrm{f}}}\eta = \frac{\eta}{\theta_{\mathrm{s}}}\frac{D_{\mathrm{h}}}{H},$$
$$\eta = \frac{\tanh(mH)}{mH}, \quad m = \sqrt{\frac{h_{\mathrm{fs}}a_{\mathrm{fs}}}{(1-\varepsilon)k_{\mathrm{s}}}} \tag{17}$$

The L_{in} is the length of channel upstream from the pin-fin heat sink.

3. The experiments

3.1. Test apparatus and instrumentation

The experimental setup displayed in Fig. 4 was divided into four main parts: (1) air supply system; (2) test section; (3) test specimens, and (4) data acquisition system. The air compressor (MITSUISEIKI 10 HP) blew air into the air tank. Then, the air flowed through a filter to remove the oil, water and particles. Finally, the air entered the test section after it passed through the straightener made of an unheated porous specimen. The air flow rate was controlled by an electric digital flowmeter with the range of 0–1000 l/min. The test section was made of 20-mm-thick Bakelite. The dimensions of the channel section were constant in height ($H = 23.7$ mm) and various in width (W). The in-line square pin-fin heat sinks, whose dimensions and porous properties are shown as samples 3 and 5 in Table 1, were situated in the test channel with two equal-spacing bypass passages beside them. These pin-fin heat sinks were made of aluminum 6061. A film heater was fixed on the bottom surface of the heat sink. The wall heat flux supplied to the film heater from the electronic power was 0.53–1.68 W/cm^2 for 32.5–250 l/min flow rate.

Eleven OMEGA T-TT-30 thermocouples for measuring the average wall temperature were embedded on the bottom surface of the heat sink. The ambient temperature, the air temperature at the channel inlet and the air temperature at the channel outlet were also monitored by other thermocouples. All thermocouples were connected to the data recorder (YOKOGAWA DA100), which will transform the potential difference signal into a temperature value. All the temperature data printed out by the data

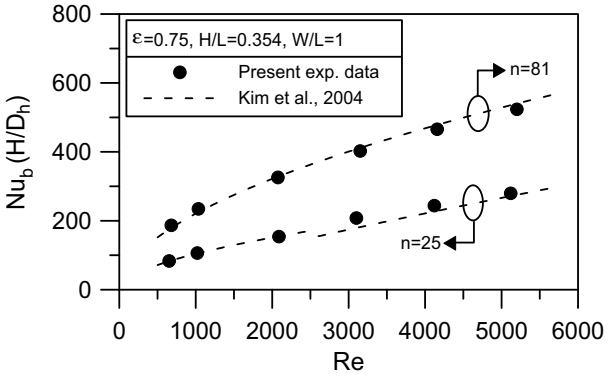

(a) Comparing experimental data with other's data

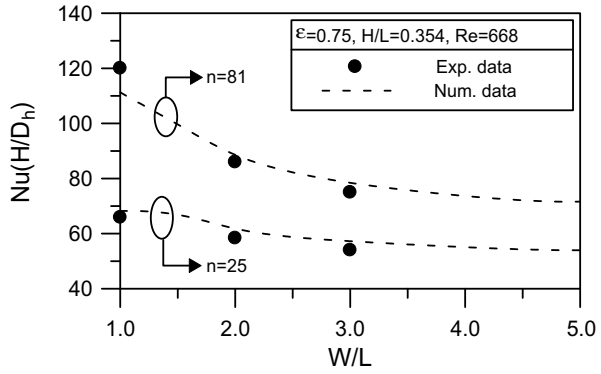

(b) Comparing numerical results with experimental data (Nusselt number)

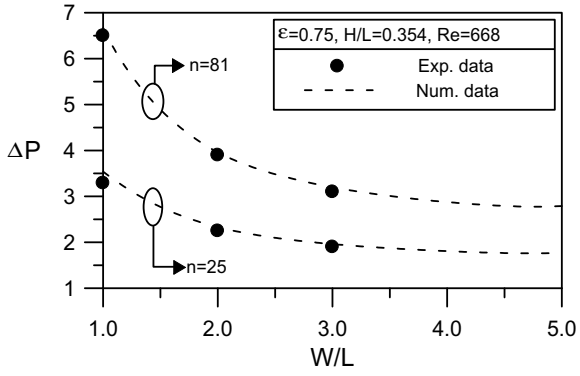

(c) Comparing numerical results with experimental data (pressure drop)

Fig. 5. Experimental validation.

recorder then are inputted into the computer and converted into data for further analysis. The inlet air temperature was about 27 °C. The temperature difference of air between inlet and outlet was about 12–17 °C. The average wall temperatures were about 64 to 75 °C. The system was assumed to be in a steady state when the temperature varied by no more than 0.2 °C in 25 min.

3.2. Uncertainty analysis

The maximum error in the flow rate was about ±5.0% at 50 l/min. The errors in the temperature measurements were resulted from the inaccuracies in the recorder readings (about ±0.2 °C). The maximum errors in determining the heat flux (q_w), the dimensions of the test channel (H and W), and relevant properties (μ and k_f) were estimated within ±6%, ±1% and ±1%, respectively. Uncertainties in parameters were estimated by using the root-sum-square method of Kline and McClintock [22] and Moffat [23]. The experimental data obtained herein revealed that the uncertainties in the Reynolds number and the Nusselt number (as shown in Eqs. (14,16,17)) were ±5.8% and ±6.7%, respectively.

4. Results and discussion

The study proposed a porous model to numerically investigate the side-bypass effect on the fluid flow and heat

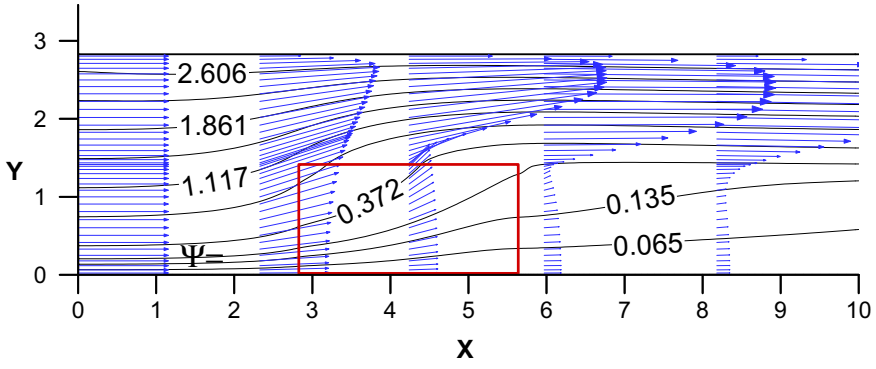

(a) sample 1 (n=81, ε=0.358)

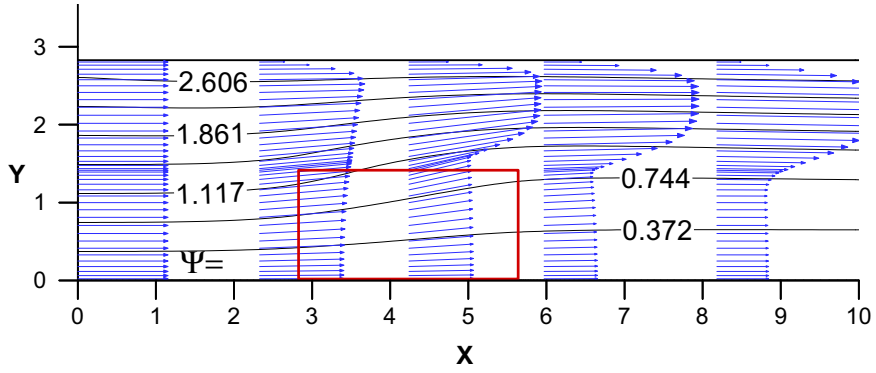

(b) sample 3 (n=81, ε=0.750)

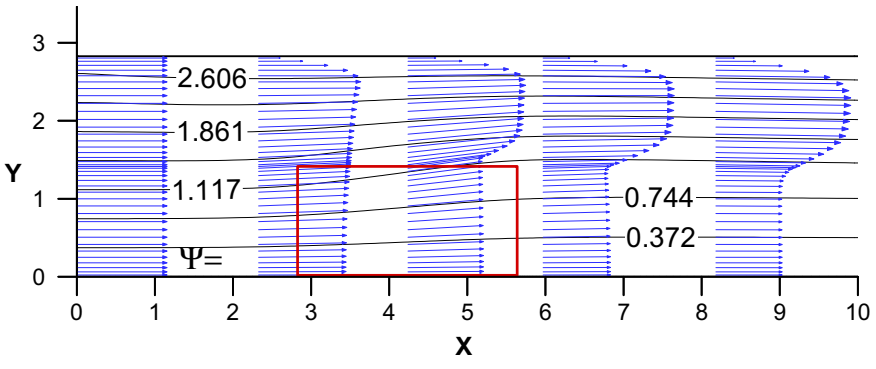

(c) sample 5 (n=25, ε=0.750)

Fig. 6. Streamlines and velocity vectors for various samples with $Re = 668$ and $W/L = 2$.

transfer of in-line square pin-fin heat sink within a rectangular channel. The relevant varied parameters were the porosity of the heat sink (ε), the number of pin-fins (n) and the wide size proportion of the channel to the heat sink (W/L). The Reynolds number was $Re = 668$.

4.1. Experimental validation

Fig. 5a shows the experimental results for the cases without side-bypass flow, and compares them with the data of Kim et al. [15]. Kim et al. [15] proposed the empirical correlation of h_{fs} (as shown in Eqs. (7,8)) for the in-line square pin-fin heat sink fully confined in a rectangular channel. The comparison results indicated that the present experimental data agree with others.

Fig. 5b displays the experimental results for the cases with side-bypass flow. Experimental results reveal that the average Nusselt numbers slowly decreased with increasing W/L as expected. The numerically predicted Nusselt numbers were also plotted in Fig. 5b. The average deviation between numerical predictions and experimental data is less than 5%, indicating that the numerical model used herein can accurately simulate the flow and thermal behavior of the pin-fin heat sink situated in a rectangular channel with laminar side-bypass flow.

4.2. Flow behaviors

Fig. 6 shows the streamlines and velocity vectors for various samples with $Re = 668$ and $W/L = 2$. As the wide size proportion of the channel to the heat sink is fixed ($W/L = 2$), the airflow entering the heat sink is mainly dependent on the penetrability of the pin-fin heat sink. As shown in Table 1, the test samples of pin-fin heat sinks studied herein covers various porosities ($\varepsilon = 0.358$–0.750) and numbers of pin-fins ($n = 25$–81, also representing the passage density in the heat sink). Using the semi-empirical formula provided by Jeng and Tzeng [16], the corresponding

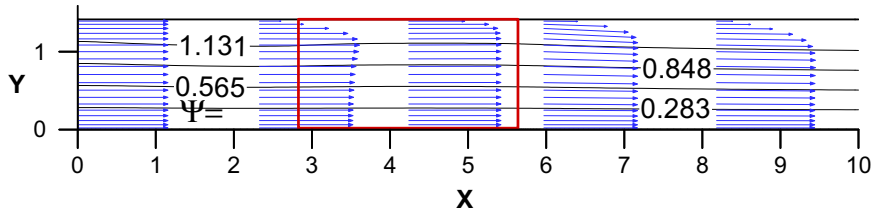

(a) W/L=1

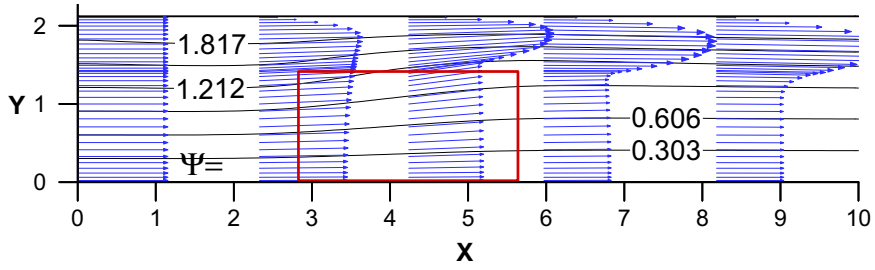

(b) W/L=1.5

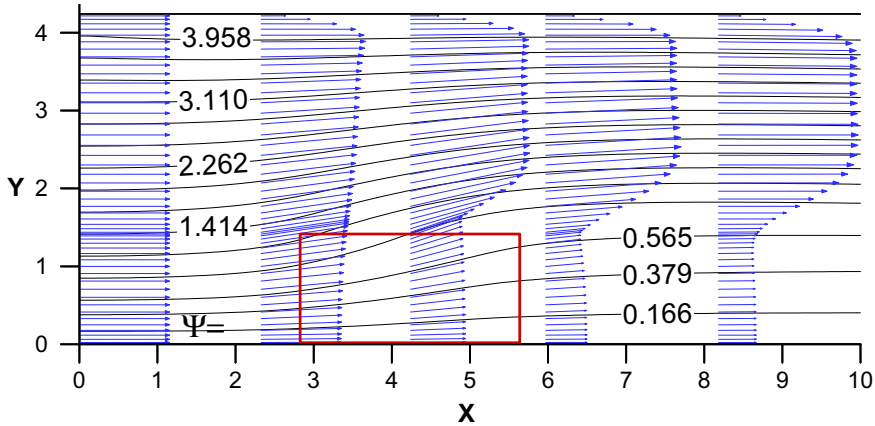

(c) W/L=3

Fig. 7. Streamlines and velocity vectors for sample 3 ($n = 81$, $\varepsilon = 0.750$) with $Re = 668$ and various W/L.

permeability (K) and the inertial coefficient (C_F) can be inferred. Table 1 and Fig. 6 show that, the larger the porosity (ε) is or the lower the n value is, the better the penetrability of the heat sink is, and there will be more airflow passing through the heat sink, which helps the forced heat convection. In addition, when the airflow enters from the windward side of the heat sink, the pin-fins will block the airflow and part of the airflow will not come out from the leeward side of the heat sink, but escape from both lateral sides of the heat sink and join into the side-bypass airflow. As the recirculation will only be generated at a far place in the downstream of the heat sink, it is not shown on the present streamlines figure. Fig. 7 presents the streamlines and velocity vectors for sample 3 ($n = 81$, $\varepsilon = 0.750$) with $Re = 668$ and various W/L. Since the porosity (ε) and the number of pin-fins (n) are fixed, the permeability (K) and the inertial coefficient (C_F) are also fixed. The airflow entering the heat sink will depend on the wide size proportion of the channel to the heat sink (W/L). It can be clearly seen from the results in Fig. 7 that, when W/L increases, the airflow bypassing both lateral sides of the heat sink will increase, and the airflow entering the heat sink will relatively decrease.

Fig. 8 shows the effects of n value, porosity (ε) and W/L on the dimensionless pressure drop (ΔP) through the pin-fin heat sink. This dimensionless pressure drop (ΔP) is estimated on the central line of the heat sink. It can be clearly seen from the result that, when the n value (number of pin-fins or the passage density in the heat sink) increases, or when the porosity (ε) or W/L decreases, the dimensionless pressure drop (ΔP) through the pin-fin heat sink will increase. This is because the airflow entering the heat sink is relatively large at small ε or W/L. It coincides with the observation on velocity vector in Figs. 6 and 7.

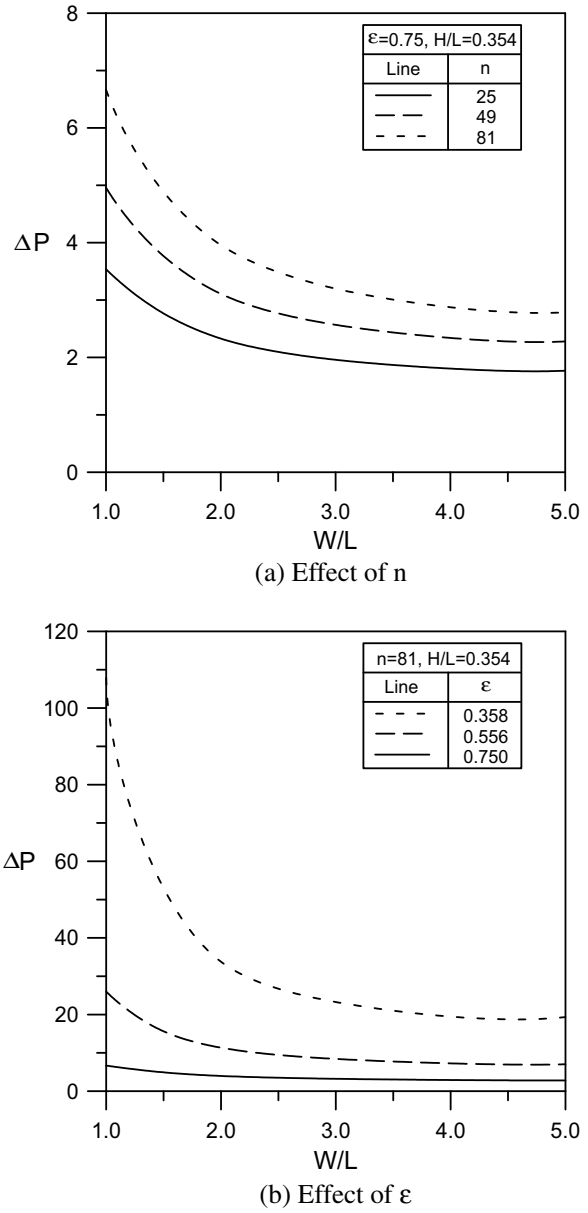

Fig. 8. Dimensionless pressure drop as a function of W/L.

4.3. Thermal characteristics

Figs. 9 and 10 depict the isotherms for typical cases with and without the side-bypass flow, respectively. The figures show a large difference between the temperature of pin-fins (θ_s) and the temperature of airflow (θ_f). Hence, during numerical simulation, it is necessary to use two-equation model for energy equation. Moreover, it can be seen from Fig. 9 that, when there are side-bypass passages, the θ_s inside the heat sink is relatively high, while the θ_s around the heat sink is relatively low. This is because the windward side of the heat sink is cooled down by the direct impact of the airflow, while the lateral and leeward sides of the heat sink enhance heat transfer due to the bypass airflow. The distribution of θ_f shows that, along the x direction, the airflow temperature (θ_f) is increased by the heat dissipated from the pin-fins. On the other hand, at the same x position, the θ_f near the lateral sides of the heat sink is lower than the θ_f inside owing to the side-bypass airflow. Fig. 10 depicts the temperature distributions of the cases without side-bypass flow. By comparing with those with side-bypass flow, the most obvious difference is that the temperatures (θ_s and θ_f) on the laterals of the heat sink are higher than the temperatures inside at the same x position. This is because the laterals of the heat sink without side-bypass flow are immediately close to the walls of the channel, the airflow speed is decreased due to the no-slip condition on the channel wall, and the heat transfer of the pin-fins in this near-wall region is naturally poor, resulting in a high θ_s. Meanwhile, owing to the decrease of airflow amount in the near-wall region, just a little heat will cause large increase of airflow temperature, resulting in a relatively high θ_f. As a whole, in cases without bypass flow, as the entire airflow goes into the heat sink, the temperature inside the heat sink is always lower than cases with bypass flow.

Fig. 11 shows the effects of n value, porosity (ε) and W/L on the average Nusselt number ($Nu(H/D_h)$) of the pin-fin

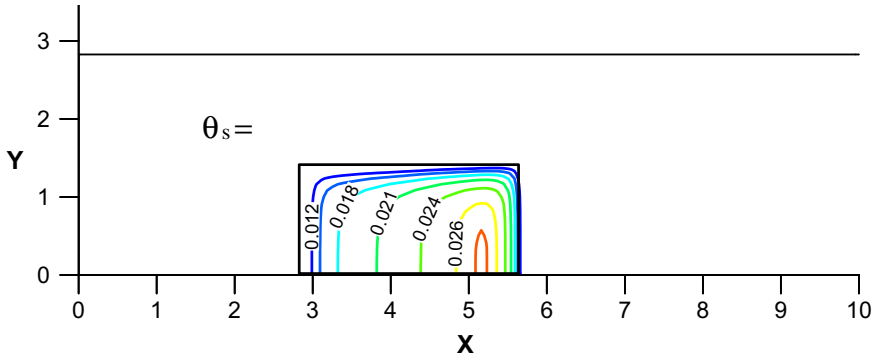

(a) Temperature of solid matrix

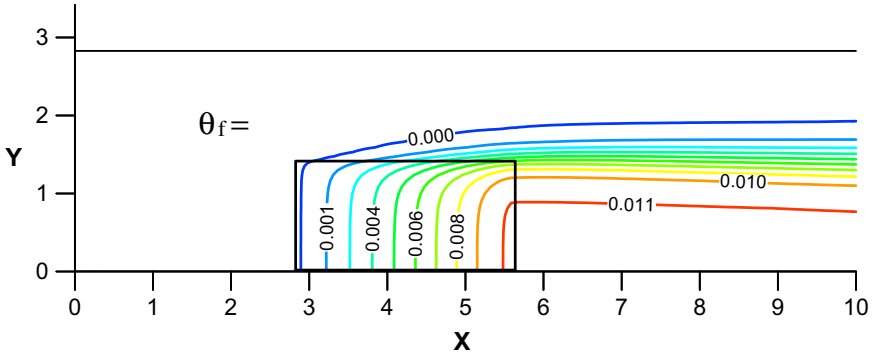

(b) Temperature of fluid stream

Fig. 9. Isotherms for sample 5 with $Re = 668$ and $W/L = 2$.

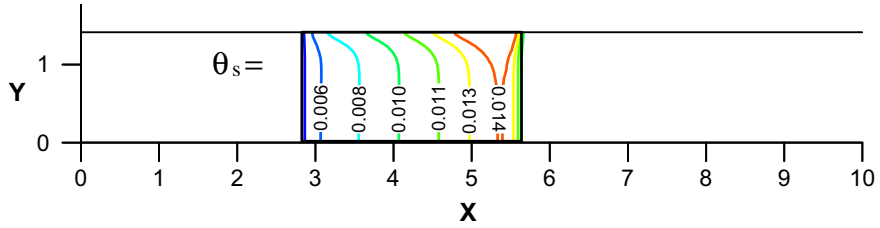

(a) Temperature of solid matrix

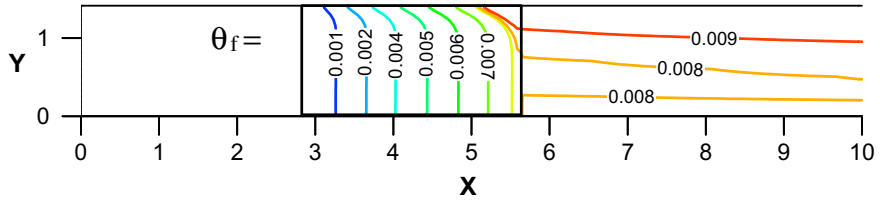

(b) Temperature of fluid stream

Fig. 10. Isotherms for sample 3 with $Re = 668$ and $W/L = 1$.

heat sink. The results indicate that the $Nu(H/D_h)$ decreases as the W/L value increases. Additionally, as expected, when $\varepsilon = 0.750$ and $W/L = 1$–5, larger n value will result in larger $Nu(H/D_h)$. This is because larger n value will cause poorer penetrability of the heat sink (but still within the magnitude order of $K = 10^{-6}m^2$), slightly decreasing the amount of airflow entering the heat sink. However, the effective area of heat dissipation of the heat sink is increased due to increase of the n value. Hence, the total heat transfer ability is increased with the increase of n value. Moreover, as shown in Fig. 11b, when n value is fixed ($n = 81$), the change of porosity ($\varepsilon = 0.358$–0.750) causes a considerable change in permeability value of the pin-fin heat sink. The permeability value increases with

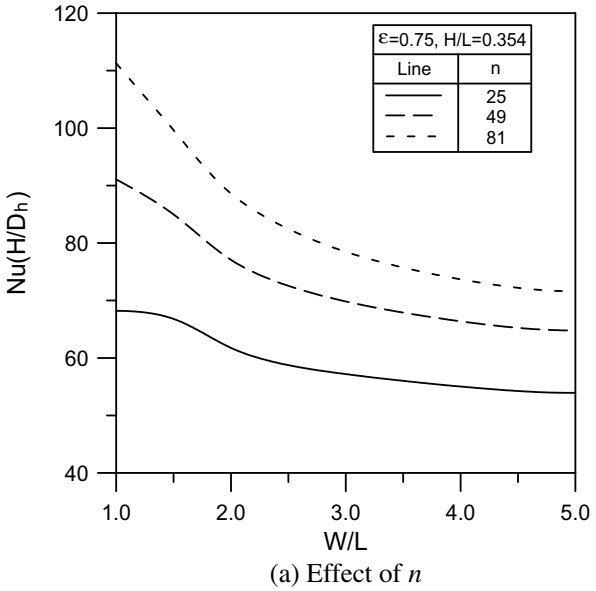

Fig. 11. Nusselt number as a function of W/L.

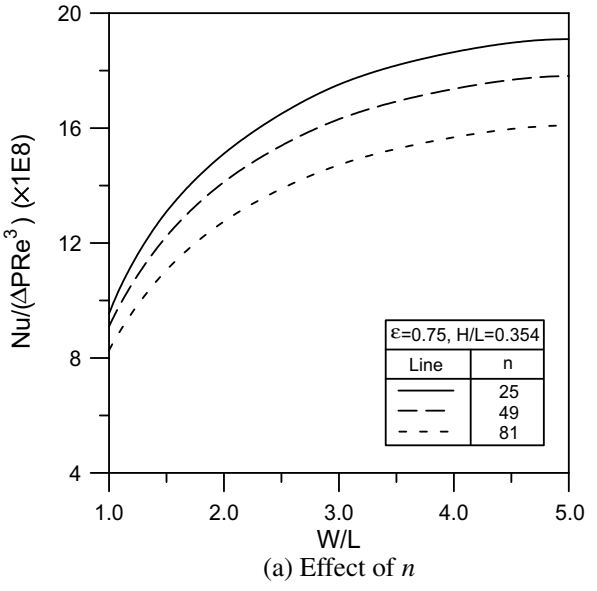

Fig. 12. Optimal cooling configuration for the maximum ratio of Nusselt number to dimensionless pumping power.

increasing the porosity. As the system with bypass flow, larger porosity presents larger amount of airflow passing through the heat sink, promoting the total heat transfer. The heat transfer enhancement due to the larger porosity is more considerable when the W/L value increases. But when the system has no bypass flow, the heat sink with same n value and various ε will have the similar $Nu(H/D_h)$. This can be explained as follows. When W/L value equals unity (no bypass flow), total airflow is forced to enter the heat sink. Although a heat sink with lower porosity will have a larger effective area of heat dissipation, its solid-to-fluid heat transfer coefficient (h_{fs}) will decrease with decreasing porosity at the same Reynolds number. Therefore, the average Nusselt number will be similar for the heat sink with same n value and various ε at $W/L = 1$.

4.4. Optimal cooling configuration

From the above analysis, it can be seen that, the larger the airflow passing through the heat sink, the better the cooling performance will be. However, the required pumping power will be higher. Hence, a better evaluation shall be based on the maximum ratio of the dissipated heat to the pumping power. In this work, assuming a constant volume of the heat sink and a constant temperature difference, the dissipated heat is proportional to Nu which is based on the area of the heated base of the pin-fin heat sink. The $(\Delta P \times Re^3)$-parameter means the pumping power. Therefore, a new parameter $Nu/(\Delta P \times Re^3)$ representing the ratio of the dissipated heat to the pumping power is introduced. Assuming a constant pumping power $(\Delta P \times Re^3)$, the bigger value of the

$Nu/(\Delta P \times Re^3)$ represents the bigger amount of the dissipated heat at a constant junction temperature difference, or means the lower junction temperature difference at a constant amount of the dissipated heat. Hence, the criteria of the optimal heat sink in the mentioned configuration (ε, n, W/L) is with the maximum value of the $Nu/(\Delta P \times Re^3)$. Fig. 12 shows the $Nu/(\Delta P \times Re^3)$ as a function of W/L for various n values and porosities (ε). The results show that an increase of W/L will lead to an increase of $Nu/(\Delta P \times Re^3)$, in particular, when $W/L = 1$–2, $Nu/(\Delta P \times Re^3)$ has a considerable increase rate along with W/L, while when $W/L = 3$–5, $Nu/(\Delta P \times Re^3)$ has a less obvious increase rate along with W/L. In addition, as shown in Fig. 12a, when $\varepsilon = 0.750$, the n value has a medium impact on $Nu/(\Delta P \times Re^3)$. In cases with $n = 25$, the $Nu/(\Delta P \times Re^3)$ is 14.5%–18.8% higher than those with $n = 81$. However, Fig. 12b shows when $n = 81$, porosity (ε) has a considerable impact on $Nu/(\Delta P \times Re^3)$. $Nu/(\Delta P \times Re^3)$ greatly increases along with the increase of porosity (ε). To sum up, within the range of present studied parameters ($0.358 \leqslant \varepsilon \leqslant 0.750$, $25 \leqslant n \leqslant 81$ and $1 \leqslant W/L \leqslant 5$), the pin-fin heat sink with $\varepsilon = 0.750$ and $n = 25$ is the optimal cooling configuration, which has a larger $Nu/(\Delta P \times Re^3)$ value. Moreover, based on medium $Nu/(\Delta P \times Re^3)$ value and suitable channel size, it is suggested that $W/L = 2$–3 is the better size ratio of channel to heat sink.

5. Conclusions

This work successfully proposed a porous model to numerically investigate the side-bypass effect on the fluid flow and heat transfer of in-line square pin-fin heat sink placed in a rectangular channel. The present porous approach employed the Brinkman–Forchheimer model for fluid flow and two-equation model for heat transfer. A configuration of in-line square pin-fin heat sink situated in a rectangular channel with fixed height ($H = 23.7$ mm), various width (W) and two equal-spacing bypass passages beside the heat sink is successfully studied. The pin-fin arrays with various porosities ($\varepsilon = 0.358$–0.750) and numbers of pin-fins ($n = 25$–81), confined within a square spreader whose side length (L) is 67 mm, are employed. Some major conclusions are summarized as follows:

(1) When the n value increases, or when the porosity (ε) or W/L decreases, the dimensionless pressure drop (ΔP) through the pin-fin heat sink will increase. Additionally, the average Nusselt number ($Nu(H/D_h)$) decreases as the W/L value increases or the n value decreases. In the case of the system with bypass flow, larger porosity (ε) promotes the total heat transfer, especially for the system with larger W/L value. But when the system has no bypass flow, the heat sink with same n value and various ε will have the similar $Nu(H/D_h)$.

(2) A new parameter $Nu/(\Delta P \times Re^3)$ representing the ratio of the dissipated heat to the pumping power is introduced. The increase of W/L will lead to increase of $Nu/(\Delta P \times Re^3)$, in particular, when $W/L = 1$–2, $Nu/(\Delta P \times Re^3)$ has a considerable increase rate along with W/L, while when $W/L = 3$–5, $Nu/(\Delta\ P \times Re^3)$ has a less obvious increase rate along with W/L. The numerical results suggest that, within the range of present studied parameters ($0.358 \leqslant \varepsilon \leqslant 0.750$, $25 \leqslant n \leqslant 81$ and $1 \leqslant W/L \leqslant 5$), the pin-fin heat sink with $\varepsilon = 0.750$ and $n = 25$ is the optimal cooling configuration based on the maximum $Nu/(\Delta P \times Re^3)$-parameter.

Acknowledgement

The author would like to thank the National Science Council of the Republic of China for financially supporting this research under Contract No. NSC 95-2221-E-344-004.

References

[1] E.M. Sparrow, J.W. Ramsey, Heat transfer and pressure drop for a staggered wall-attached array of cylinders with tip clearance, Int. J. Heat Mass Transfer 21 (1978) 1369–1377.
[2] B.A. Jubran, M.A. Hamdan, R.M. Abdualh, Enhanced heat transfer, missing pin, and optimization for cylindrical pin fin arrays, ASME J. Heat Transfer 115 (1993) 576–583.
[3] O.N. Sara, S. Yapici, M. Yilmaz, T. Pekdemir, Second law analysis of rectangular channels with square pin-fins, Int. Commun. Heat Mass Transfer 28 (2001) 617–630.
[4] O.N. Sara, Performance analysis of rectangular ducts with staggered square pin fins, Energy Convers. Manage. 44 (2003) 1787–1803.
[5] M.B. Dogruoz, M. Urdaneta, A. Ortega, Experiments and modeling of the hydraulic resistance and heat transfer of in-line square pin fin heat sinks with top by-pass flow, Int. J. Heat Mass Transfer 48 (2005) 5058–5071.
[6] M.B. Dogruoz, A. Ortega, R.V. Westphal, A model for flow bypass and tip leakage in pin fin heat sinks, ASME J. Electron. Packaging 128 (2006) 53–60.
[7] W.S. Fu, H.C. Huang, W.Y. Liou, Thermal enhancement in laminar channel flow with a porous block, Int. J. Heat Mass Transfer 39 (1996) 2165–2175.
[8] A.M. Morega, A. Bejan, S.W. Lee, Free stream cooling of a stack of parallel plates, Int. J. Heat Mass Transfer 38 (1995) 519–531.
[9] S. Narasimhan, J. Majdalani, Compact heat sink simulations in both forced and natural convection flows, in: Proceedings of Eighth AIAA/ASME Joint Thermophysics and Heat Transfer Conference, AIAA 2002-3212, 2002, pp. 24–26.
[10] S.J. Kim, D. Kim, Forced convection in microstructures for electronic equipment cooling, ASME J. Heat Transfer 121 (1999) 639–645.
[11] D. Kim, S.J. Kim, Compact modeling of fluid flow and heat transfer in straight fin heat sinks, ASME J. Electron. Packaging 126 (2004) 247–255.
[12] E. Yu, Y. Joshi, Heat transfer enhancement from enclosed discrete components using pin-fin heat sinks, Int. J. Heat Mass Transfer 45 (2002) 4957–4966.
[13] H.I. You, C.H. Chang, Determination of flow properties in non-Darcian flow, ASME J. Heat Transfer 119 (1997) 190–192.
[14] H.I. You, C.H. Chang, Numerical prediction of heat transfer coefficient for a pin-fin channel flow, ASME J. Heat Transfer 119 (1997) 840–843.
[15] D. Kim, S.J. Kim, A. Ortega, Compact modeling of fluid flow and heat transfer in pin fin heat sinks, ASME J. Electron. Packaging 126 (2004) 342–350.

[16] T.M. Jeng, S.C. Tzeng, A semi-empirical model for estimating permeability and inertial coefficient of pin-fin heat sinks, Int. J. Heat Mass Transfer 48 (2005) 3140–3150.
[17] J.P. Holman, Heat Transfer, Mcgraw-Hill, New York, 1990, pp. 32–33.
[18] P.J. Roache, Computational Fluid Dynamics, Hermosa, Albuquerque, New Mexico, 1972, pp. 139–173.
[19] S.V. Patankar, Numerical Heat Transfer and Fluid Flow, McGraw Hill–Hemisphere, New York, 1980, pp. 113–137.
[20] P.C. Huang, K. Vafai, Analysis of forced convection enhancement in a channel using porous blocks, J. Thermophys. Heat Transfer 8 (1994) 563–573.
[21] S.L. Lee, A strong implicit solver for two-dimensional elliptic differential equations, Numer. Heat Transfer Part B 16 (1989) 161–178.
[22] S.J. Kline, F.A. Mcclintock, Describing uncertainties in single-sample experiments, Mech. Eng. (1953) 3–8.
[23] R.J. Moffat, Contributions to the theory of single-sample uncertainty analysis, ASME J. Fluids Eng. 104 (1986) 250–260.